

Changes in the Na D₁ Absorption Components of η Carinae Provide Clues on the Location of the Dissipating Central Occulter

CONNOR S. PICKETT,¹ NOEL D. RICHARDSON,¹ THEODORE GULL,^{2,3} D. JOHN HILLIER,⁴ HENRIK HARTMAN,⁵
NOUR IBRAHIM,^{1,6} ALEXIS M. LANE,¹ EMILY STRAWN,¹ AUGUSTO DAMINELI,⁷ ANTHONY F. J. MOFFAT,⁸
FELIPE NAVARETE,⁹ AND GERD WEIGELT¹⁰

¹*Department of Physics and Astronomy, Embry-Riddle Aeronautical University, 3700 Willow Creek Road, Prescott, AZ 86301, USA*

²*Exoplanets and Stellar Astrophysics Laboratory, NASA/Goddard Space Flight Center, Greenbelt, MD 20771*

³*Space Telescope Science Institute, 3700 San Martin Drive. Baltimore, MD 21218, USA*

⁴*Department of Physics and Astronomy and the Pittsburgh Particle Physics, Astrophysics, and Cosmology Center (PITT PACC), University of Pittsburgh, 3941 O'Hara Street, Pittsburgh, PA 15260, USA*

⁵*Department of Materials Science and Applied Mathematics, Faculty of Technology and Society, Malmö University, SE-20506 Malmö, Sweden*

⁶*Department of Astronomy, University of Michigan, 1085 S. University, Ann Arbor, MI 48109, USA*

⁷*Universidade de São Paulo, Instituto de Astronomia, Geofísica e Ciências Atmosféricas, Rua do Matão 1226, Cidade Universitária, São Paulo, Brasil*

⁸*Département de Physique and Centre de Recherche en Astrophysique du Québec (CRAQ) Université de Montréal, C.P. 6128, Succ. Centre-Ville, Montréal, Québec, H3C 3J7, Canada*

⁹*SOAR Telescope/NSF's NOIRLab, Avda Juan Cisternas 1500, 1700000, La Serena, Chile*

¹⁰*Max Planck Institute for Radio Astronomy, Auf dem Hügel 69, D-53121 Bonn, Germany*

ABSTRACT

The Na D absorption doublet in the spectrum of η Carinae is complex, with multiple absorption features associated with the Great Eruption (1840s), the Lesser Eruption (1890s), and interstellar clouds. The velocity profile is further complicated by the P Cygni profile originating in the system's stellar winds and blending with the He I λ 5876 profile. The Na D profile contains a multitude of absorption components, including those at velocities of -145 km s^{-1} , -168 km s^{-1} , and $+87 \text{ km s}^{-1}$ that we concentrate on in this analysis. Ground-based spectra recorded from 2008 to 2021 show significant variability of the -145 km s^{-1} absorption throughout long-term observations. In the high ionization phases of η Carinae prior to the 2020 periastron passage, this feature disappeared completely but briefly reappeared across the 2020 periastron, along with a second absorption at -168 km s^{-1} . Over the past few decades, η Car has been gradually brightening demonstrated to be caused by a dissipating occulter. The decreasing absorption of the -145 km s^{-1} component, coupled with similar trends seen in absorptions of ultraviolet resonant lines, indicate that this central occulter was possibly a large clump associated with the Little Homunculus or another clump between the Little Homunculus and the star. We also report on a foreground absorption component at $+87 \text{ km s}^{-1}$. Comparison of Na D absorption in the spectra of nearby systems demonstrates that this red-shifted component likely originates in an extended foreground structure consistent with a previous ultraviolet spectral survey in the Carina Nebula.

Keywords: Massive stars (732), Binary stars (154), Luminous blue variable stars (944), Ejecta (453), Circumstellar matter (241)

1. INTRODUCTION

Luminous Blue Variables (LBVs) are evolved massive stars that are near the Eddington Limit, and are variable on time scales of days to centuries. The variability of these stars is such that when the star is observed being hotter, it is fainter in the optical and brighter in the ultraviolet. The majority of active LBVs tend

to fluctuate between spectral types of late-O or early B- and F-type supergiants, while maintaining a nearly constant bolometric luminosity, with only small changes (see for example the work on AG Car; Groh et al. 2009, 2011). These stars have been observed to have stellar eruptions where they eject up to several solar masses of material, creating circumstellar ejecta around many of these objects. The population of LBVs was recently documented in Richardson & Mehner (2018) and their properties have been reviewed in the past by Humphreys & Davidson (1994) and van Genderen (2001).

η Carinae (η Car; HD 93308; HR 4210; previously η Argus) is a massive binary star within the Carina Nebula and is sometimes considered a prototype of the LBVs. The system is relatively close to us with a distance of approximately only 2.3 kpc (Smith 2006). η Car has undergone two observed eruptions, causing significant amounts of gas and other debris to obscure the system itself, although there may have been additional eruptions in the past (Kiminki et al. 2016). This material has resulted in a bipolar shell of ejecta surrounding the system from the Great Eruption in the 1840s and from the second Lesser Eruption in the 1890s, known as the Homunculus and the Little Homunculus, respectively. The binary is in a long-period 5.54 year orbit (2022.7 ± 0.3 d; Damineli 1996; Damineli et al. 1997; Teodoro et al. 2016) that is highly eccentric ($e = 0.9$; e.g., Damineli et al. 2000; Grant et al. 2020; Grant & Blundell 2022). The primary star provides some ionization to the surrounding gas, such as causing Fe II emission lines, while the secondary star further ionizes the Homunculus and Little Homunculus. During the system’s periastron passage, the secondary star passes into the far side of the optically thick wind of the primary star, which causes the ionization of gas in our line of sight to drop to normal levels for the primary star. This variability, where the ionization of the gas temporarily drops, has been referred to as spectroscopic events in the literature. As noted in several studies (e.g., Melnick et al. 1982; Damineli et al. 1998; Davidson et al. 2005; Johansson et al. 2005; Gull et al. 2006; Richardson et al. 2010, 2015), the change in ionization causes increased absorption of low-ionization species from the ejecta, especially at velocities associated with the Little Homunculus (near -145 km s $^{-1}$).

In recent years, the central source of the η Carinae system has been observed to be brightening. Unlike most normal LBV activity such as the S Doradus cycles, the central source is brightening in both the optical and ultraviolet in tandem. There are two competing hypotheses related to this variability. The first is that

the central star is quickly evolving as it settles from the Great Eruption (Mehner et al. 2010, 2011, 2015, 2019; Davidson et al. 2018; Martin et al. 2021). This suggestion relies on wind lines, such as H α (Mehner et al. 2010), changing with a long-term evolution, which could be interpreted as changes in the mass-loss properties. The second hypothesis is that there was an clump in the line of sight that has been dissipating and/or moving out of our line of sight (Hillier & Allen 1992; Hillier et al. 2001; Damineli et al. 2019, 2021). This is supported by the large amount of added extinction that is needed in the models of the stellar spectra by both Hillier et al. (2001, 2006) and Groh et al. (2012). As this extinction was fairly grey, a change in the extinction should allow most wavelengths to change at similar rates.

We aimed to use the variability of the Na D absorption component associated with the Lesser Eruption to understand how it relates to the documented changes in the spectrum of η Carinae. The ionization potential of neutral Na is ≈ 5.14 eV which corresponds to a wavelength of ~ 2412 Å. Thus the ionization of neutral sodium is achieved by radiation in the near ultraviolet. However the ground state photoionization cross-section of Na I has a Cooper minimum¹ near 2000 Å², and consequently a large fraction of the ionizations will occur by radiation shortward of 1800 Å. Given the large ultraviolet flux of η Car, we expect Na to mostly singly ionized. As a consequence the time variation of the Na I equivalent widths will be primarily governed by the time scale for the flux variations, and thus the orbital time scale around periastron. Thus we would expect the Na equivalent width (\propto column density) variations, and the ultraviolet flux variations to track each other. In Section 2, we describe 12 years of observations of the system from the Cerro Tololo Inter-American Observatory (CTIO) 1.5 m telescope and its echelle spectrographs, along with some complementary observations from the *Hubble Space Telescope* and the Space Telescope Imaging Spectrograph (*HST*/STIS). Section 3 details the measurements we made of three absorption components in the Na D spectrum. Section 4 discusses these findings, and we conclude this study in Section 5.

2. OBSERVATIONS

¹ A Cooper minimum is a region where the photoionization cross-section approaches zero, and is typically exhibited by alkali elements (Cooper 1962; Pradhan & Nahar 2011)

² The Na I photoionization data were computed by K T Taylor for the Opacity project (Seaton 1987) and were obtained from <http://cdsweb.u-strasbg.fr/topbase/home.html>

Our observations come from a time-series of high-resolution spectroscopy of η Car taken with the CTIO 1.5 m SMARTS (Small and Moderate Aperture Research Telescope System) telescope. All data were taken with a fiber centered on the object, with a projected angular size of $2.7''$. The first observations were taken in 2008–2010 with the fiber-fed spectrograph having a resolving power of $R \sim 40,000$, and were described by Richardson et al. (2010, 2015). Since the 2009 periastron passage, a time-series of higher signal-to-noise and higher resolution spectra were obtained with the SMARTS telescope and the new CHIRON spectrograph with modes having a resolving power of $80,000 - 90,000$ for these observations (Tokovinin et al. 2013; Paredes et al. 2021). For the CHIRON time-series, the data were described by Richardson et al. (2016), with more observations having the same characteristics being taken in the intervening time, especially around the 2020 periastron passage. In total, we analyze 418 spectra taken with the CTIO 1.5 m telescope in this study.

Data were previously reduced for all data previously published using techniques described in Richardson et al. (2010, 2015) for the fiber echelle. This was done with standard techniques using IRAF³. For the CHIRON data, the data were processed with the standard pipeline described recently by Paredes et al. (2021). The observations also included a standard observation of HR 4468 (B9.5Vn) or μ Col (O9.5V), which was used to empirically derive the blaze function and then remove this through division with custom scripts in either IDL or with python. This was done in orders without spectral lines, with the remaining orders (primarily around H α or H β) were interpolated to match adjacent orders.

The observations of the most recent periastron passage began with CTIO/CHIRON data collected on 15 October 2019 and concluded with data collected on 18 March 2020 when the telescope was closed due to the COVID-19 pandemic. These new observations did provide higher signal-to-noise Na D profiles than ever before, owing to the ongoing increase in the visual brightness of η Car (e.g., Damineli et al. 2019, 2021).

In order to study the Na D complex, we first had to remove contamination from water in Earth’s atmosphere. We utilized the telluric measurements from Wallace & Livingston (2003) to construct a telluric tem-

plate at the same resolution and sampling rate as the CHIRON data. This template could then be artificially strengthened or weakened to match each spectrum, under the assumption that the relative strengths of different lines remains fixed. This method was used over the entire Na D region, including regions with no intrinsic features from η Carinae to ensure that the remaining spectrum was intrinsic to the source and the intervening material from the ejecta and the interstellar medium.

When dealing with spectra of η Car, it is important to use a reliable clock with which we can compare observations to the binary ephemeris. To that end, we adopt the ephemeris from Teodoro et al. (2016), which should be close to the timing of periastron in 2014, and is given by the equation relating the phase ϕ to the heliocentric julian date (HJD) by

$$\phi = \frac{(HJD - 2,456,874.4)}{2022.7} + 13.$$

In this context, the addition of the 13 in the equation means that the 2014 periastron was the thirteenth observed spectroscopic minimum since the first reported by Gaviola (1953).

We found an absorption component which we suspected to be interstellar in its origin, and we collected spectra of neighboring stars with the same high-resolution mode of the CHIRON spectrograph in July 2021. The objects observed were HD 93204, HD 93205, HD 303308, and CPD 59° 2628. Using the same methodology as with η Car, the spectra were reduced and telluric corrected.

We also used archived spectra taken with the *Hubble Space Telescope*/Space Telescope Imaging Spectrograph (HST/STIS) in the E140M echelle mode with a nominal resolving power, $R=45,800$. The three spectra were recorded at phases $\phi = 11.119, 13.194$ and 14.170 , which is in the early recovery to the high-ionization state of the nebular structures. These data were pipeline-processed and then downloaded from MAST.

3. ABSORPTION COMPONENTS AT VARIOUS VELOCITIES

In Fig. 1, we show selected spectra from our time-series of the system. There are several features in this figure, which we will describe in detail in the following section. The interstellar components near 0 km s^{-1} (and near -300 km s^{-1} for the Na D₂ component in the shown Na D₁ reference frame) are both very close to black in our data, but some small uncorrectable amount of scattered light in the spectrographs makes the profile appear to have a minimum near 1% of the normalized continuum light.

³ IRAF was distributed by the National Optical Astronomy Observatories, which is operated by the Association of Universities for Research in Astronomy, Inc., under contract to the National Science Foundation.

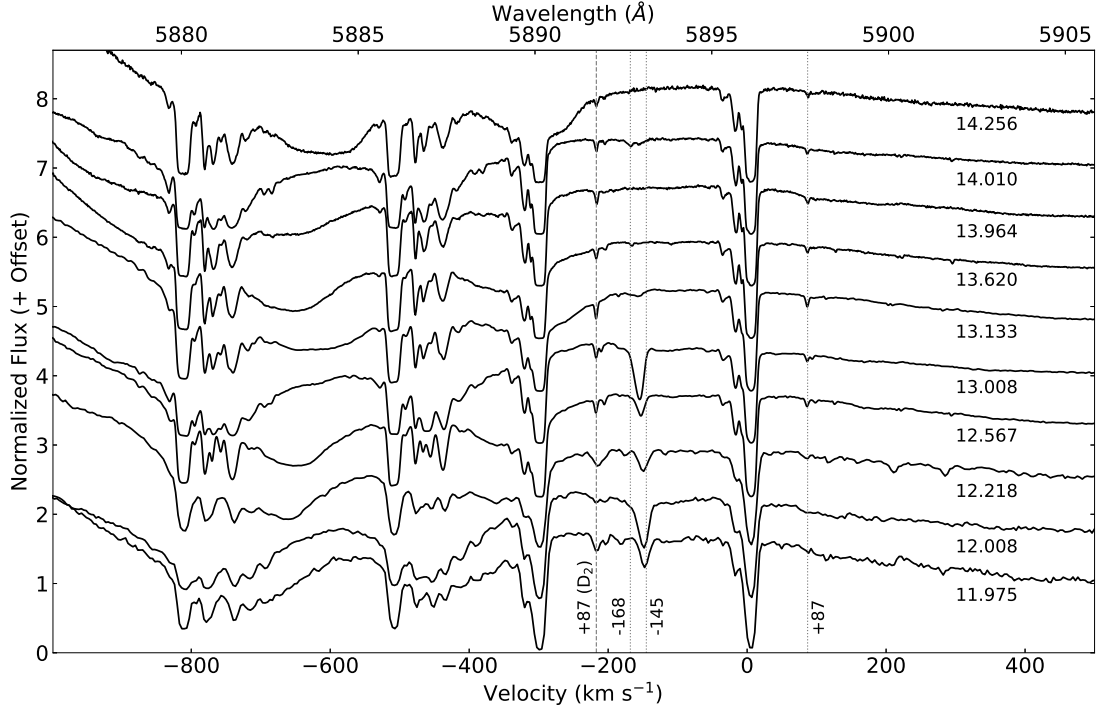


Figure 1. A subset of the data taken for η Carinae, from phase $\phi = 11.975$ to $\phi = 14.256$ (indicated as numbers below the spectra on the right), which highlights some of the variations seen in the data. The dotted lines represent the multiple absorption features discussed in this paper relative to the Na D₁ line, with the +87 km s⁻¹ component also shown as a dashed line for the Na D₂ line. We indicate the velocity of the absorptions at the bottom of the figure. The data before phase 12.5 were taken with the lower-resolution fiber-fed echelle spectrograph, while the more recent data were taken with the CHIRON spectrograph. The variable emission on the red side of this plot is from He I $\lambda 5876$, for which the variability changes the apparent spacing on the left.

There is a dramatic disappearance of a feature at -145 km s⁻¹ over our full data set. This and other velocities were fit for a radial velocity by means of a Gaussian profile or by measuring the point of minimum flux on select data sets with high signal-to-noise. We caution that these profiles are not always simple Gaussians, so we adopt these velocities to better describe the variations of the individual components. Richardson et al. (2010) described a similar component in the H α profile that appeared and strengthened across the 2009 periastron passage, and Richardson et al. (2015) noted changes in the Na D complex similar to those of H α during the 2009 periastron passage. In the most recent periastron passage, the feature’s center has moved to bluer velocities, and the profile has bifurcated so that a second component at -168 km s⁻¹ is now visible near periastron. Furthermore, there is a component at $+87$ km s⁻¹ that is seen in all of the CHIRON spectra, without much variability present. For our analysis, we concentrate on the Na D₁ $\lambda 5896$ line, as the Na D₂ $\lambda 5890$ line is strongly

blended with both the D₁ components originating in the Homunculus and the He I $\lambda 5876$ line.

For the features that we discuss in this paper, we measure the equivalent width defined as

$$W_\lambda = \int \frac{F_C(\lambda) - F_\lambda(\lambda)}{F_C(\lambda)} d\lambda,$$

where F_C is the continuum flux and F_λ is the flux as a function of wavelength (λ). The continuum around these features is difficult to define as the normalized spectrum shows broad Na D emission from the outer portions of the stellar wind. Therefore, we re-normalized each observation around the feature to measure the strength at that time of the observation. In order to estimate the errors in W_λ of the measurements, we adopted the method of Vollmann & Eversberg (2006), where the error depends on the dispersion of the spectrum ($\Delta\lambda$), the number of spectral pixels integrated over (n), and the signal-to-noise ratio (SNR) of the spectrum per resolution element by the equation

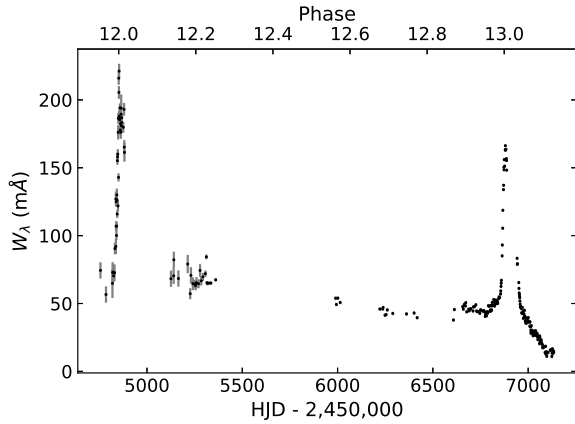


Figure 2. The measured equivalent width strength of the -145 km s^{-1} feature, in reference to Na D₁, through the 2009 and 2014 events, where the strength increases drastically near the two periastron passages. In the interim time, the feature is seen to have a slow decline, which accelerates to higher velocities after the 2014 event.

$$\sigma = \frac{n\Delta\lambda - W_\lambda}{SNR}.$$

The errors for the weak feature at -168 km s^{-1} appear to be a bit larger than the scatter around the trends in the points even when we carefully measured the quantities needed in the equation above. Such a trend could mean that we over-estimated the errors, however since we had to locally normalize the data around the feature, within the emission component of the Na D complex, there are additional errors involved in that process. There are also sources of error that are not accounted for, such as how the strength could change on a changing slope of the emission profile. We have therefore kept these error bars at this level, since a measurement to a precision of $< 5 \text{ mÅ}$ is difficult to achieve with the star and this instrument.

3.1. The Absorption Component at -145 km s^{-1}

Richardson et al. (2015) found that the absorption component near -145 km s^{-1} increases near the periastron passage, similar to the H α component that strengthens at the same time (Richardson et al. 2010; Daminieli et al. 2021). We measured these spectra, along with the CTIO/CHIRON data, in the region surrounding the variable -145 km s^{-1} feature. The exact range changed with time as the feature moved to bluer velocities in more recent observations, but the range of integration was typically about 25 km s^{-1} wide and moved with the absorption with time. The equivalent width measurements are tabulated in the online appendix (Table 1). Gull et al. (2006) reported that ultraviolet features of this velocity seemed to appear stronger at peri-

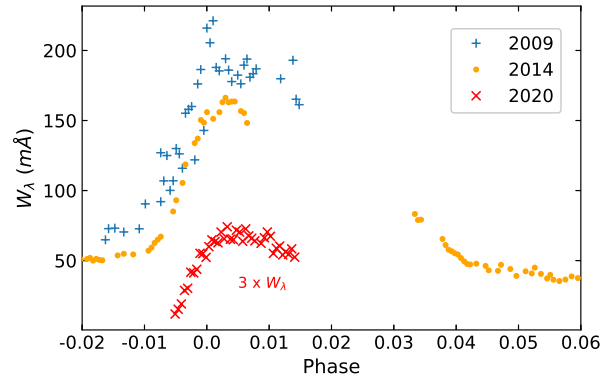


Figure 3. The measured equivalent width strength of the -145 km s^{-1} feature through the 2009, 2014, and 2020 events, phased to the binary clock. For the 2020 event, the equivalent width of the blended components at -145 and -168 km s^{-1} were measured, but multiplied by a factor of 3 to be displayed on a similar scale as the previous two periastron passages.

astron, yet remain fairly consistent in equivalent width (W_λ) throughout the remainder of the orbit.

From our long time-series of measurements in Fig. 2, the absorption at -145 km s^{-1} is observed to be weakening over this time period. In Fig. 1 we see that this feature seems to move to bluer velocities over this same time period, while the interstellar absorption components stay constant in velocity as expected. By a time shortly after the 2014 periastron event, this feature was indiscernible in the spectra despite the higher signal-to-noise ($S/N \sim 150\text{--}200$ per pixel). We see similarities in the two events for 2009 and 2014 when phased to the binary clock (Fig. 3). The change in the ultraviolet flux during the periastron passage is about a factor of three according to Gull et al. (2021), consistent with the changes seen in this line. The 2020 event is discussed in the following subsection.

It was reported in Gull et al. (2006) that the -145 km s^{-1} features in the ultraviolet would change intensity across the spectroscopic minimum. The absorption feature in Fe II, as measured at $\phi = 0.739$, appears during the broad maximum. However, when at a minimum, the feature appeared stronger and was also accompanied by two more features at velocities near -145 km s^{-1} . As noted by Gull et al. (2006), this indicates a brief drop in ionization of the Little Homunculus in our line of sight caused by the shadowing of that region by the primary's wind intervening in front of the secondary star.

3.2. The Absorption Component at -168 km s^{-1}

During the recent 2020 periastron passage, an absorption component at -168 km s^{-1} has appeared. This

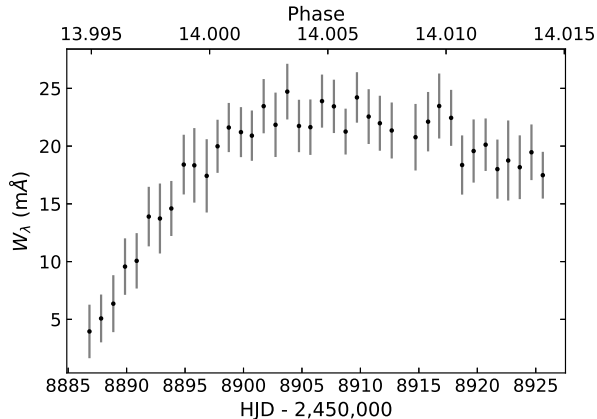


Figure 4. The measured equivalent width strength of the -168 km s^{-1} feature across the 2020 periastron passage, where the strength increases after periastron. This measurement is a blend of the bluer component of the -145 km s^{-1} with the -168 km s^{-1} component.

absorption may have been present in earlier periastra, but would have been blended with a much stronger component at -145 km s^{-1} . It was also seen in the $\text{H}\alpha$ line as observed by [Damineli et al. \(2021\)](#), although at the velocity of -180 km s^{-1} . This change in the $\text{H}\alpha$ and Na D absorptions associated with the periastron passages is likely due to a changing ionization structure in the Little Homunculus. A similar velocity component was reported in low-ionization ultraviolet lines by [Gull et al. \(2006\)](#) during the low-state corresponding to the periastron passages. This component, while independent of the -145 km s^{-1} feature, seems to have become similar in strength to its changing-velocity counterpart at -145 km s^{-1} , and could have been undetected in previous cycles due to the stronger component at -145 km s^{-1} . We compare the blended component to that of the -145 km s^{-1} component in [Fig. 3](#), where we see that the beginning of the increase in absorption shows a similar time from the pre-event minimum to maximum as the previous events.

While not as prominent as the -145 km s^{-1} feature had been, the -168 km s^{-1} feature became significantly strong enough to take equivalent width measurements during the last periastron. Measurements for the -168 km s^{-1} feature were taken between the wavelengths of 5892.45\AA and 5893.20\AA , corresponding to the radial velocities of $-180.82 \text{ km s}^{-1}$ and $-142.62 \text{ km s}^{-1}$ respectively. This integration includes the smaller contribution of the -145 km s^{-1} component remnants, which can both be seen in the spectrum at phase 14.010 in [Fig. 1](#). We attempted to measure the two features at -145 and -168 km s^{-1} independently, but the features were blended and weak and non-Gaussian in nature.

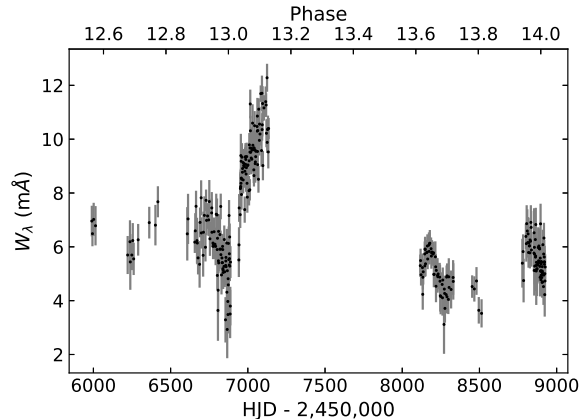


Figure 5. The measured equivalent width strength of the $+87 \text{ km s}^{-1}$ feature from the CHIRON spectrograph, where the strength changes slightly near the 2014 periastron, presumably because of the changing profile of the occulter.

The resulting measurements were deemed unreliable by both their component errors and visual inspection of the spectra compared with the measurements.

As seen in [Fig. 4](#), there is variability in W_λ of the -168 km s^{-1} feature. This originates in a decreasing level of ionization near periastron. The increased activity near $\phi = 14.00$ resulted in the steady climb in magnitude of W_λ , which then begins to decrease near $\phi = 14.018$. This process is similar to that of the -145 km s^{-1} feature. The timing of the disappearance of the -168 km s^{-1} feature was interrupted by the temporary closure of the facilities at CTIO.

3.3. The Absorption Component at $+87 \text{ km s}^{-1}$

Following telluric correction, a previously-unnoticed absorption component was recognized at $\sim +87 \text{ km s}^{-1}$. This component, seen in [Figure 1](#), indicates that material is moving towards η Car and would represent an inflow of material if originating in the gas surrounding η Car. A second, identical component at -217 km s^{-1} in the Na D₁ reference frame is also observed and represents the Na D₂ transition at the same velocity.

Equivalent width measurements for the $+87 \text{ km s}^{-1}$ feature were taken between the wavelengths of 5897.55\AA and 5897.74\AA , corresponding to the radial velocities of 78.87 km s^{-1} and 88.53 km s^{-1} and are shown in [Fig. 5](#). Each measurement was made within the bounds of $.19\text{\AA}$, or 9.66 km s^{-1} . We notice a small change around the 2014 periastron passage, which may be explained by the change in the V-band brightness across periastron such as that observed by [Damineli et al. \(2019\)](#). In this regard, we see an increase in continuum flux leading up to the event, followed by a dip in the flux after periastron. With the equivalent width depending on the continuum,

as shown by the associated equivalent width equation earlier in this section, we see that the small differences at that time can be explained by the change in flux. Furthermore, oscillations at times away from periastron may reflect changes in the photometric brightness, such as those recently documented by Richardson et al. (2018). However, as noted by Richardson et al. (2010), usually changes in the equivalent widths due to the continuum are primarily a concern for large flux lines such as the H α line. It is also possible that these small changes are due to changes in the Na D emission in the region of this absorption component, which could alter our measurements. The exact amount of variation that could be intrinsic to this component should therefore be very small when compared to the large changes in the underlying flux from the system along with the variability of the broad Na D wind emission features present in this region of the spectrum.

4. DISCUSSION

Our measurements of Na D₁ absorption components from η Carinae can be used to illuminate some recent changes in the spectrum and photometric record. In particular, Damineli et al. (2019, 2021) found that there are long-term changes related to the circumstellar extinction in the line of sight that should conclude in ~ 2032 . Our results show that the Na D absorption from the Little Homunculus is much weaker and likely absent at times away from periastron, in broad agreement with the results from Damineli et al. (2019). The spectral modeling of the system, first accomplished with *HST* spectroscopy and the CMFGEN non-LTE radiative transfer code by Hillier & Miller (1998); Hillier et al. (2001), required 2.0 magnitudes of grey extinction in the line of sight to model both the stellar (wind) spectrum and achieve the correct line strengths for the narrow line emission from the surrounding Weigelt knots, but also had 5 magnitudes of extinction in *V*-band in the line of sight towards the binary. We show a cartoon diagram of the most likely geometry that could accommodate the observations in Fig. 6.

If we assume that the component near -145 km s^{-1} originates in the Little Homunculus as noted in several studies (e.g., Melnick et al. 1982; Damineli et al. 1998; Davidson et al. 2005; Johansson et al. 2005; Gull et al. 2006; Richardson et al. 2010, 2015), then we can begin to interpret the variability and character of the components at -145 and -168 km s^{-1} . First, we consider the variability of the component at -145 km s^{-1} . Richardson et al. (2010) describe the variability of the component at the same velocity for the H α transition. For H α , Richardson et al. (2010) postulate that dur-

ing the spectroscopic minimum near periastron, the secondary star would pass behind the primary, and thus drop the ionizing radiation in our line of sight. This drop in ionization would then relax the gas and allow lower ionization transitions to be observed in absorption.

These same principles can explain the changes we see in both the -145 km s^{-1} component (Fig. 2) across the 2009 and 2014 periastron passages and the -168 km s^{-1} component (Fig. 4) during the recent 2020 periastron event. The -168 km s^{-1} absorption was only previously observed in six low-ionization lines (Mg I, Mg II, Cr II, Mn II, Fe II, and Ni II) in the near ultraviolet by Gull et al. (2006) and only during the low-ionization state of the binary. In contrast, the -145 km s^{-1} was observed in the same lines, as well as in He I, Ti II, V II, Co II, and Ni II, although Gull et al. (2006) reported it as -146 km s^{-1} .

In the far-ultraviolet, several transitions have been observed by *HST*/STIS, allowing us to make comparisons to the Na D₁ observations described here. For this discussion, we limit ourselves to the Al II $\lambda 1671$, Al III $\lambda 1855$, Si II $\lambda 1527$, and Si IV $\lambda 1394$ transitions which were observed during the previous two periastron passages where we also have CHIRON spectroscopy. All of these ultraviolet transitions and Na D are resonance lines. In Fig. 7, we show these transitions at phases 11.119, 13.194, and 14.170 so that the binary-induced phase differences are minimal, and we can examine the long-term evolution of the profiles. Each profile was normalized to the ‘continuum’ flux level near 1483\AA recorded at phase $\phi = 14.170$. Gull et al. (2022, in prep) demonstrate that normalization of the ‘continuum’ is valid since virtually all continuum originates from deep within η Car-A.

These profiles show that these species have evolved to show less absorption at -145 km s^{-1} , although these changes are amplified because the normalization of these data. This shows a similar trend as the Na D observations, where recent observations since phase ~ 13.5 have had no absorption present at that velocity except for a brief appearance at the cycle 14 periastron event. During the recent periastron, this absorption was seen at higher velocity and with a companion absorption component at -168 km s^{-1} . In the ultraviolet profiles, the lower ionization Al II and Si II lines show that the absorption components at these velocities are also seen at higher velocities than in earlier cycles, such as just following the cycle 11 periastron passage.

We postulate that the absorption component was formed in a spatially unresolved dense clump within the Little Homunculus. This clump would respond to

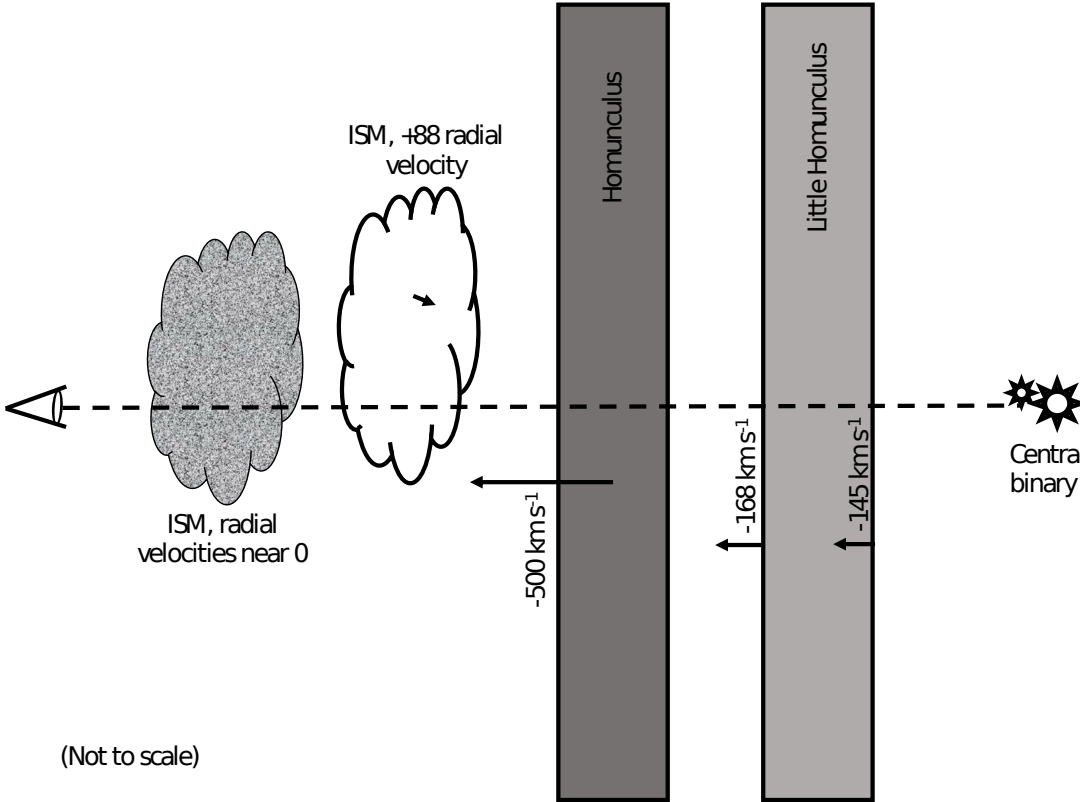


Figure 6. A cartoon diagram showing the geometry of the gas that provides Na D absorption. A detailed discussion of this geometry is in the text.

the ionization changes induced by the companion’s orbit around the primary star. In this situation, the clump would be either moving out of our line of sight or dissipating with time. Both scenarios allow for a weaker absorption profile now than in the past, consistent with the observations of the ultraviolet resonance lines and the Na D profiles.

We used a curve of growth method to find the column density of the absorbing Na atoms during the times of just prior to the 2009 event (phases near 11.95), near phase 12.5, and after the 2014 event at phase 13.1. We used these times to avoid times when the ionization changes, which would therefore change the column density of neutral sodium in our line of sight. At these three epochs, the equivalent widths were roughly 70 ± 12 mÅ, 52 ± 2.5 mÅ, and 14.7 ± 2.2 mÅ respectively. With the known oscillator strength and wavelength of Na D₁, we can then calculate the values of W_λ/λ to obtain the values of $F(\tau)$ using the curve of growth from Spitzer (1978) with an assumed line width of 10 km s^{-1} , which is complimentary to techniques used for the local interstellar medium (Welsh et al. 1990). Then, we derive a column density of $4.9 \times 10^{11} \text{ cm}^{-2}$, $3.5 \times 10^{11} \text{ cm}^{-2}$, and $0.8 \times 10^{11} \text{ cm}^{-2}$ for these three epochs respectively, confirming the lower column density in recent times. This

is in agreement with the changes in the ultraviolet flux which has increased by about a factor of 10 in the same time period (Gull et al. 2021).

With a clump in the line of sight, we can also imagine that the angular size was relatively small to us. The neighboring Weigelt knots, separated from the central source by only about $0.2''$ (Weigelt & Ebersberger 1986), did not undergo the same amount of extinction as the central source according to the models of Hillier et al. (2001). As a result, an angularly small clump similar to the Weigelt knots, either within the Little Homunculus or in our line of sight could provide the necessary extinction to provide the absorption lines and the added extinction toward the binary. As Damineli et al. (2019, 2021) have noted, the central occulter must be dissipating to explain the object’s brightening and the lack of observed changes in the object’s spectrum. As a result, the simplicity of a dissipating or moving clump in our line of sight would help explain many of the unusual observations of this system, although neither explanation can be fully refuted with the current data.

The component at -145 km s^{-1} is also seen to shift in its velocity during the last several cycles as it was dissipating. The movement of the clump out of the line-of-sight or its thicker parts dissipating on the interior of

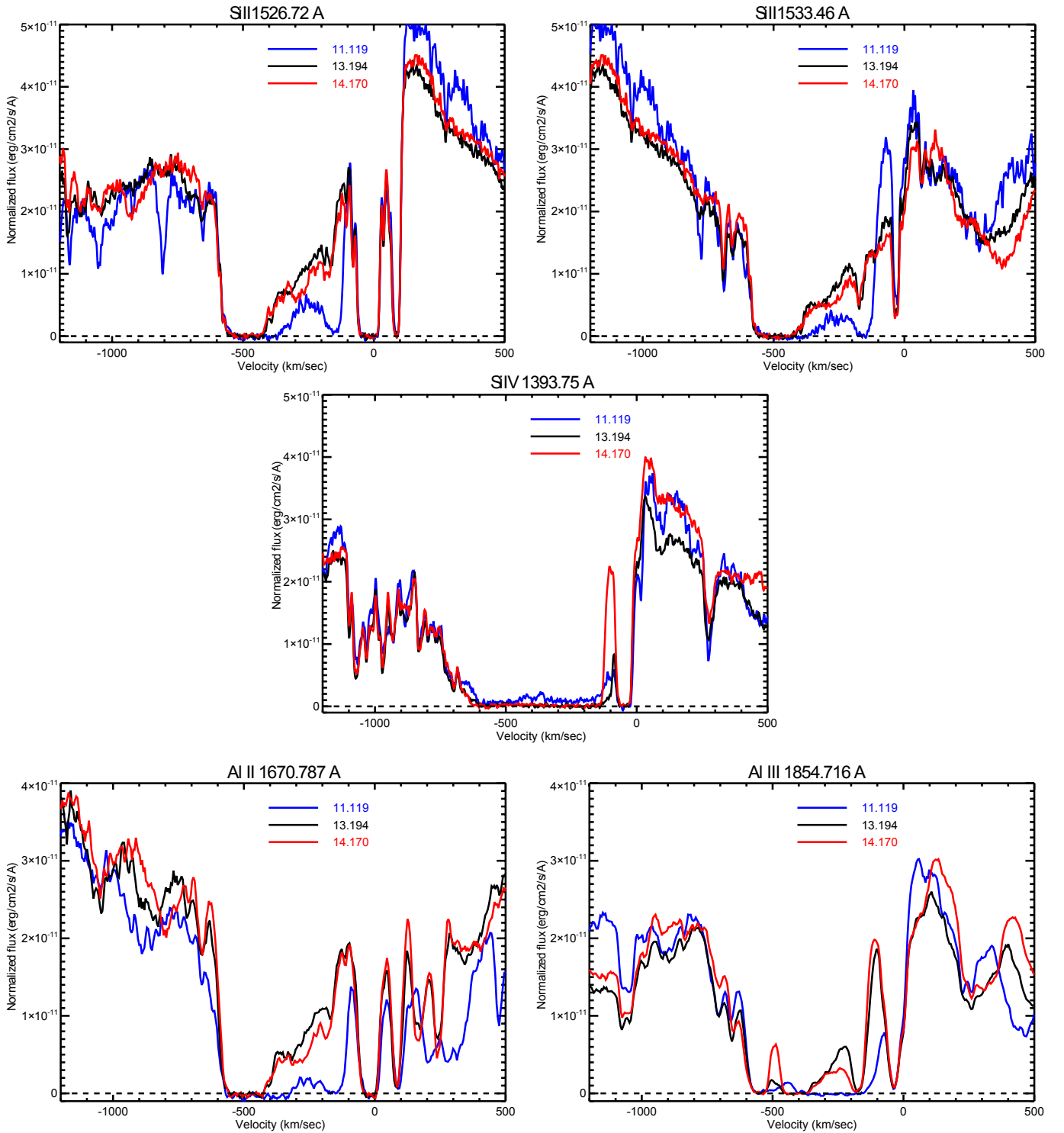


Figure 7. Velocity profiles of Si II, Si IV, Al II and Al III resonant lines as recorded by *HST*/STIS. The three spectra were recorded at similar phases following periastron passages 11, 13 and 14 when η Carinae has re-entered the high-ionization state. Long-term changes in the Little Homunculus are apparent between -100 and -400 km s⁻¹. The absorption at $+87$ km s⁻¹ is also present in the low ionization Si II and Al II profiles.

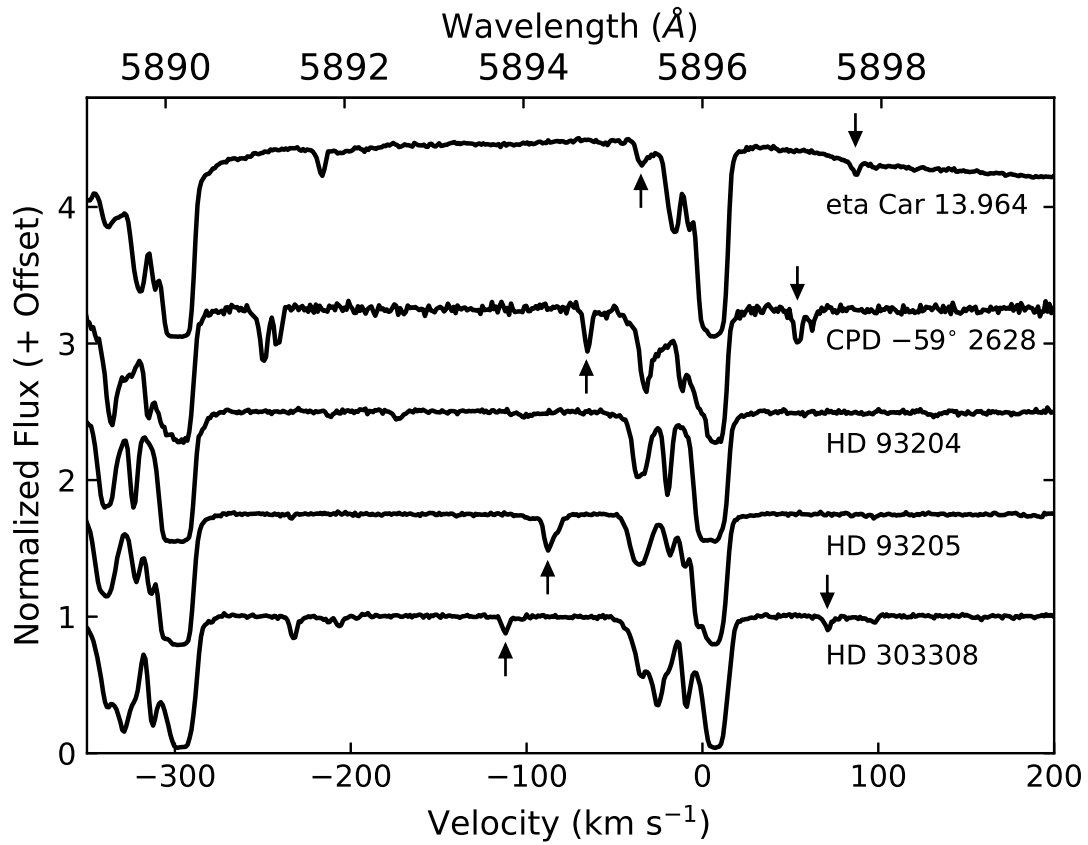


Figure 8. A comparison of the Na D profiles of η Carinae at $\phi = 13.964$, CPD $-59^\circ 2628$, HD 93204, HD 93205, and HD 303308 at 1 arcmin to north. η Carinae, CPD $-59^\circ 2628$, and HD 303308 clearly have features present at positive velocities similar to that of η Car. Similar interstellar features are denoted with arrows.

the Little Homunculus shell, as illustrated in our Fig. 6, would allow for an apparent shift in the radial velocity of the component by having the densest part of the clump being at different points in the outflow of the Little Homunculus. Furthermore, as the thickest part of the clump at the central velocity of the clump dissipated or moved out of the line of sight, the changing ionization front would penetrate into the Little Homunculus allowing for the weaker -168 km s^{-1} to be visible during the most recent periastron passage while not observed in Na D in past events.

Moreover, Gull et al. (2016) recently reported on spatially resolved *HST*/STIS spectroscopy of the binary across an entire orbit of the system. The results indicate that the Weigelt knot B (A4 in the analysis of Weigelt & Ebersberger 1986) has fully dissipated or disappeared in the surrounding region of η Carinae. If the clump is similar ejecta as the Weigelt knots that were ejected during the Lesser Eruption, then the clump is traversing the region rather than dissipating, then it could now be providing additional extinction toward this clump. However, Weigelt B could also be dissipating with time, meaning that the clumps left over from the Lesser Eruption of η Car could all be beginning to dissipate around this time, as the Weigelt knots have been shown to be associated with the Lesser Eruption of η Carinae (Weigelt & Kraus 2012).

The origin of the component at $+87 \text{ km s}^{-1}$ is simpler to explain. With an apparent lack of variability (Fig. 5), it is hard to envision a situation in which that component would actually represent inflowing material from the surrounding winds and ejecta. We anticipated this being interstellar in origin so we tested our hypothesis in two ways. First, we see in the low-ionization lines of Al II and Si II that there is a component at roughly the same velocity as the $+87 \text{ km s}^{-1}$ component of Na D₁ and Na D₂. This component is not seen to vary in its absolute absorption with the *HST* observations recorded over an interval of 16.5 years (Fig. 7). The $+87 \text{ km s}^{-1}$ component is not present in Si IV $\lambda 1394$, Al III $\lambda 1855$ nor in Si II $\lambda 1533$. The absorbing cloud contains only singly-ionized ions and is sufficiently cool that no Si II ions populate the low-lying energy level at 287 cm^{-1} .

These features were reminiscent of the ultraviolet lines of other stars in the Carina Nebula complex observed by Walborn et al. (2002). Strong absorption has been previously observed in the nearby CPD -59°2603, as noted in Danks et al. (2001). Small line widths of high-velocity features, as well as column density variations, indicate structures with transverse velocities when compared to radial velocities. Walborn et al. (2002) depicts these absorptions from both 1997 and 1999 observations. These

data show, in total, nine strong, low-ionization absorptions within our line of sight. The strongest features appear in lower-velocity regions, but it should be noted that dominant components of high-ionization states appear at intermediate and negative velocities. The high-ionization absorption corresponds to the global expansion of the H II region. This expansion is further investigated in Walborn et al. (2007). These observations of neutral sodium at varying velocities for stars in the Carina Nebula raise the possibility that they are formed in low-density outflowing gas from the region, perhaps originating from a past supernova or the collective winds of the cluster.

To further test the interstellar origin of this component, we observed three of the Carina stars observed by Walborn et al. (2002) with the CHIRON spectrograph at the same resolving power as our η Carinae observations, along with CPD -59° 2628 which is very close to η Car in the sky⁴. For these observations of Na D shown in Fig. 8, we see many similarities in the interstellar lines.

The primary interstellar lines near 0 km s^{-1} all show similar components for these stars. As noted by Walborn et al. (2002), many of these stars have lines at high velocities. The Na D components of the neighboring CPD -59°2603 show a positive velocity component at lower velocity than that of η Carinae, with a similar profile showing a double absorption. The observations of η Car show a similar double component of absorption. These similarities with other stars within the Carina Nebula show that they could be explained by a complicated foreground absorption complex, perhaps from a past supernova or cluster wind that shows complexity across the region, but the physical cause for these complex interstellar absorptions is beyond the scope of this paper.

5. CONCLUSIONS

Our study of the Na D complex of η Carinae has found several interesting trends that relate to other observations of the system.

- The absorption component near -145 km s^{-1} has been observed to move to higher negative velocities over the past decade. Simultaneously, the strength of this absorption has weakened overall, becoming indiscernible by 2018. This happened in parallel to the brightening of the star while the nebula has remained more consistent in its brightness. This

⁴ CPD -59° 2628 was seen to interfere with η Car's photometric light curve observed by *BRITTE-Constellation* reported by Richardson et al. (2018) due to its close proximity in the sky.

points to the central occulter being a spatially unresolved clump in the Little Homunculus.

- We find a new absorption in the spectra that is near $+87 \text{ km s}^{-1}$ which seems to be interstellar in origin. Similarly shaped structures are seen in neighboring stars, but at different velocities. The variability of this component can likely be attributed to changes in the continuum flux and Na D wind emission during the periastron passages.
- The interstellar feature at $+87 \text{ km s}^{-1}$ is also seen in some low-ionization ultraviolet resonance lines.
- To further disentangle if the occulter is/was in the Little Homunculus or another clump interior to the Little Homunculus, future observations of the Na profile at high resolution and in reflected light from various lines of sight in the Homunculus could illuminate this discussion.

ACKNOWLEDGEMENTS

Many measurements in this project were originally made by Lucas St-Jean, and we thank him for these early contributions that led to these results. The CTIO observations are the result of many allocations of telescope time. We thank internal SMARTS allocations at Georgia State University (in 2008–2009), as well as NOIR Lab (formerly NOAO) allocations of NOAO-09B-153, NOAO-12A-216, NOAO-12B-194, NOAO-13B-328, NOAO-15A-0109, NOAO-18A-0295, NOAO-19B-204, NOIRLab-20A-0054, and NOIRLab-21B-0334. C.S.P. and A.L. were partially supported by the Embry-Riddle Aeronautical University Undergraduate Research Institute. E.S. acknowledges support from the Arizona Space Grant program. N.D.R., C.S.P., A.L., E.S., and T.R.G. acknowledge support from the *HST* GO Programs #15611 and #15992. A.F.J.M. is grateful to NSERC (Canada) for financial aid.

REFERENCES

- Cooper, J. W. 1962, *Physical Review*, 128, 681, doi: [10.1103/PhysRev.128.681](https://doi.org/10.1103/PhysRev.128.681)
- Damineli, A. 1996, *ApJL*, 460, L49, doi: [10.1086/309961](https://doi.org/10.1086/309961)
- Damineli, A., Conti, P. S., & Lopes, D. F. 1997, *NewA*, 2, 107, doi: [10.1016/S1384-1076\(97\)00008-0](https://doi.org/10.1016/S1384-1076(97)00008-0)
- Damineli, A., Kaufer, A., Wolf, B., et al. 2000, *ApJL*, 528, L101, doi: [10.1086/312441](https://doi.org/10.1086/312441)
- Damineli, A., Stahl, O., Kaufer, A., et al. 1998, *A&AS*, 133, 299, doi: [10.1051/aas:1998461](https://doi.org/10.1051/aas:1998461)
- Damineli, A., Fernández-Lajús, E., Almeida, L. A., et al. 2019, *MNRAS*, 484, 1325, doi: [10.1093/mnras/stz067](https://doi.org/10.1093/mnras/stz067)
- Damineli, A., Navarete, F., Hillier, D. J., et al. 2021, *MNRAS*, 505, 963, doi: [10.1093/mnras/stab1398](https://doi.org/10.1093/mnras/stab1398)
- Danks, A. C., Walborn, N. R., Vieira, G., et al. 2001, *ApJL*, 547, L155, doi: [10.1086/318897](https://doi.org/10.1086/318897)
- Davidson, K., Ishibashi, K., Martin, J. C., & Humphreys, R. M. 2018, *ApJ*, 858, 109, doi: [10.3847/1538-4357/aabdef](https://doi.org/10.3847/1538-4357/aabdef)
- Davidson, K., Martin, J., Humphreys, R. M., et al. 2005, *AJ*, 129, 900, doi: [10.1086/427132](https://doi.org/10.1086/427132)
- Gaviola, E. 1953, *ApJ*, 118, 234, doi: [10.1086/145746](https://doi.org/10.1086/145746)
- Grant, D., & Blundell, K. 2022, *MNRAS*, 509, 367, doi: [10.1093/mnras/stab3057](https://doi.org/10.1093/mnras/stab3057)
- Grant, D., Blundell, K., & Matthews, J. 2020, *MNRAS*, 494, 17, doi: [10.1093/mnras/staa669](https://doi.org/10.1093/mnras/staa669)
- Groh, J. H., Hillier, D. J., & Damineli, A. 2011, *ApJ*, 736, 46, doi: [10.1088/0004-637X/736/1/46](https://doi.org/10.1088/0004-637X/736/1/46)
- Groh, J. H., Hillier, D. J., Damineli, A., et al. 2009, *ApJ*, 698, 1698, doi: [10.1088/0004-637X/698/2/1698](https://doi.org/10.1088/0004-637X/698/2/1698)
- Groh, J. H., Hillier, D. J., Madura, T. I., & Weigelt, G. 2012, *MNRAS*, 423, 1623, doi: [10.1111/j.1365-2966.2012.20984.x](https://doi.org/10.1111/j.1365-2966.2012.20984.x)
- Gull, T. R., Kober, G. V., & Nielsen, K. E. 2006, *ApJS*, 163, 173, doi: [10.1086/500113](https://doi.org/10.1086/500113)
- Gull, T. R., Madura, T. I., Teodoro, M., et al. 2016, *MNRAS*, 462, 3196, doi: [10.1093/mnras/stw1829](https://doi.org/10.1093/mnras/stw1829)
- Gull, T. R., Navarete, F., Corcoran, M. F., et al. 2021, *ApJ*, 923, 102, doi: [10.3847/1538-4357/ac22a6](https://doi.org/10.3847/1538-4357/ac22a6)
- Hillier, D. J., & Allen, D. A. 1992, *A&A*, 262, 153
- Hillier, D. J., Davidson, K., Ishibashi, K., & Gull, T. 2001, *ApJ*, 553, 837, doi: [10.1086/320948](https://doi.org/10.1086/320948)
- Hillier, D. J., & Miller, D. L. 1998, *ApJ*, 496, 407, doi: [10.1086/305350](https://doi.org/10.1086/305350)
- Hillier, D. J., Gull, T., Nielsen, K., et al. 2006, *ApJ*, 642, 1098, doi: [10.1086/501225](https://doi.org/10.1086/501225)
- Humphreys, R. M., & Davidson, K. 1994, *PASP*, 106, 1025, doi: [10.1086/133478](https://doi.org/10.1086/133478)
- Johansson, S., Gull, T. R., Hartman, H., & Letokhov, V. S. 2005, *A&A*, 435, 183, doi: [10.1051/0004-6361:20041193](https://doi.org/10.1051/0004-6361:20041193)
- Kiminki, M. M., Reiter, M., & Smith, N. 2016, *MNRAS*, 463, 845, doi: [10.1093/mnras/stw2019](https://doi.org/10.1093/mnras/stw2019)
- Martin, J. C., Davidson, K., Humphreys, R. M., & Ishibashi, K. 2021, *Research Notes of the American Astronomical Society*, 5, 197, doi: [10.3847/2515-5172/ac1fff](https://doi.org/10.3847/2515-5172/ac1fff)
- Mehner, A., Davidson, K., Humphreys, R. M., et al. 2010, *ApJL*, 717, L22, doi: [10.1088/2041-8205/717/1/L22](https://doi.org/10.1088/2041-8205/717/1/L22)

- Mehner, A., Davidson, K., Martin, J. C., et al. 2011, *ApJ*, 740, 80, doi: [10.1088/0004-637X/740/2/80](https://doi.org/10.1088/0004-637X/740/2/80)
- Mehner, A., Davidson, K., Humphreys, R. M., et al. 2015, *A&A*, 578, A122, doi: [10.1051/0004-6361/201425522](https://doi.org/10.1051/0004-6361/201425522)
- Mehner, A., de Wit, W. J., Asmus, D., et al. 2019, *A&A*, 630, L6, doi: [10.1051/0004-6361/201936277](https://doi.org/10.1051/0004-6361/201936277)
- Melnick, J., Ruiz, M. T., & Maza, J. 1982, *A&A*, 111, 375
- Paredes, L. A., Henry, T. J., Quinn, S. N., et al. 2021, *AJ*, 162, 176, doi: [10.3847/1538-3881/ac082a](https://doi.org/10.3847/1538-3881/ac082a)
- Pradhan, A. K., & Nahar, S. N. 2011, *Atomic Astrophysics and Spectroscopy*
- Richardson, N. D., Gies, D. R., Gull, T. R., Moffat, A. F. J., & St-Jean, L. 2015, *AJ*, 150, 109, doi: [10.1088/0004-6256/150/4/109](https://doi.org/10.1088/0004-6256/150/4/109)
- Richardson, N. D., Gies, D. R., Henry, T. J., Fernández-Lajús, E., & Okazaki, A. T. 2010, *AJ*, 139, 1534, doi: [10.1088/0004-6256/139/4/1534](https://doi.org/10.1088/0004-6256/139/4/1534)
- Richardson, N. D., & Mehner, A. 2018, *Research Notes of the American Astronomical Society*, 2, 121, doi: [10.3847/2515-5172/aad1f3](https://doi.org/10.3847/2515-5172/aad1f3)
- Richardson, N. D., Madura, T. I., St-Jean, L., et al. 2016, *MNRAS*, 461, 2540, doi: [10.1093/mnras/stw1415](https://doi.org/10.1093/mnras/stw1415)
- Richardson, N. D., Pablo, H., Sterken, C., et al. 2018, *MNRAS*, 475, 5417, doi: [10.1093/mnras/sty157](https://doi.org/10.1093/mnras/sty157)
- Seaton, M. J. 1987, *Journal of Physics B Atomic Molecular Physics*, 20, 6363, doi: [10.1088/0022-3700/20/23/026](https://doi.org/10.1088/0022-3700/20/23/026)
- Smith, N. 2006, *ApJ*, 644, 1151, doi: [10.1086/503766](https://doi.org/10.1086/503766)
- Spitzer, L. 1978, *Physical processes in the interstellar medium*, doi: [10.1002/9783527617722](https://doi.org/10.1002/9783527617722)
- Teodoro, M., Daminieli, A., Heathcote, B., et al. 2016, *ApJ*, 819, 131, doi: [10.3847/0004-637X/819/2/131](https://doi.org/10.3847/0004-637X/819/2/131)
- Tokovinin, A., Fischer, D. A., Bonati, M., et al. 2013, *PASP*, 125, 1336, doi: [10.1086/674012](https://doi.org/10.1086/674012)
- van Genderen, A. M. 2001, *A&A*, 366, 508, doi: [10.1051/0004-6361:20000022](https://doi.org/10.1051/0004-6361:20000022)
- Vollmann, K., & Eversberg, T. 2006, *Astronomische Nachrichten*, 327, 862, doi: [10.1002/asna.200610645](https://doi.org/10.1002/asna.200610645)
- Walborn, N. R., Danks, A. C., Vieira, G., & Landsman, W. B. 2002, *ApJS*, 140, 407, doi: [10.1086/339373](https://doi.org/10.1086/339373)
- Walborn, N. R., Smith, N., Howarth, I. D., et al. 2007, *PASP*, 119, 156, doi: [10.1086/511756](https://doi.org/10.1086/511756)
- Wallace, L., & Livingston, W. 2003, *An atlas of the solar spectrum in the infrared from 1850 to 9000 cm⁻¹ (1.1 to 5.4 micrometer)*
- Weigelt, G., & Ebersberger, J. 1986, *A&A*, 163, L5
- Weigelt, G., & Kraus, S. 2012, in *Astrophysics and Space Science Library*, Vol. 384, *Eta Carinae and the Supernova Impostors*, ed. K. Davidson & R. M. Humphreys, 129, doi: [10.1007/978-1-4614-2275-4_6](https://doi.org/10.1007/978-1-4614-2275-4_6)
- Welsh, B. Y., Vedder, P. W., & Vallergera, J. V. 1990, *ApJ*, 358, 473, doi: [10.1086/169001](https://doi.org/10.1086/169001)

APPENDIX

A. ONLINE TABLES

Table 1. – 145 km s⁻¹ Measurements

HJD	W_λ	σ
-2,450,000		
(d)	(mÅ)	(mÅ)
4755.8605	74.4100	6.0000
4784.8577	56.6100	6.0000
4818.8060	64.8500	10.7695
4819.8108	72.8200	7.6075
4821.8520	73.1500	6.1266
4824.7536	70.4100	4.5138
4829.7838	72.7000	6.0701
4831.7530	90.4600	4.2639
4836.7382	127.0000	5.5035
4836.7510	92.0700	5.6323
4837.7318	106.9000	3.6945
4838.7569	125.0000	3.4637
4839.7867	100.1000	3.3596
4840.7789	107.0000	3.2727
4841.7684	130.0000	4.6655
4842.7738	126.2000	2.6296
4843.7735	115.9000	2.8100
4844.7762	155.2000	3.0682
4845.7651	158.0000	3.4639
4846.7704	160.0000	3.7042
4847.7971	121.9000	4.0158
4848.7409	176.1000	5.2701
4849.7256	186.4000	4.1598
4850.7334	142.9000	3.0279
4851.7190	216.0000	4.8571
4852.7420	205.5000	4.6979
4853.7283	221.2000	5.3942
4854.7404	187.9000	4.5506
4855.7358	185.4000	3.6463
4857.7856	194.1000	3.2556
4858.7676	186.0000	3.2942
4859.7749	177.8000	3.8427
4861.7267	182.4000	2.7894

Table 1 *continued*

Table 1 (*continued*)

HJD	W_λ	σ
-2,450,000		
(d)	(mÅ)	(mÅ)
4862.7393	176.2000	4.8369
4863.7592	189.5000	2.4151
4864.7284	193.9000	10.1812
4865.7026	180.9000	4.0439
4866.7166	183.4000	3.5817
4867.7075	186.9000	3.2210
4875.6516	179.8000	4.0514
4879.6606	193.0000	4.7157
4880.6719	165.2000	5.1300
4881.6680	161.3000	6.8569
5125.8682	68.2600	6.0000
5139.8436	70.3600	6.0000
5140.8246	82.1900	6.0000
5164.8118	68.4000	6.0000
5213.7590	79.0900	6.7142
5226.7402	57.2000	4.0890
5230.6255	70.7500	6.0000
5240.6474	64.5900	4.7343
5250.6127	64.4800	3.0098
5254.5753	63.3300	3.6512
5259.6044	65.3400	4.1624
5270.5564	64.5900	3.2782
5278.4984	74.3400	4.6157
5284.5346	66.7000	3.5030
5293.5099	69.6000	3.0000
5306.5008	71.9600	2.4000
5311.5186	84.3400	1.8000
5314.5970	65.2800	1.2000
5317.4860	64.8600	1.5000
5327.4623	65.0300	1.0000
5335.4752	65.0700	1.0000
5360.3720	67.4400	1.2147
5989.6915	53.8782	1.2147
5993.7546	49.2825	1.2244
6001.7288	53.9522	1.2145
6013.6892	50.7330	1.2213
6221.8876	45.9027	1.2315
6236.8436	45.9535	1.2314
6238.8674	47.0313	1.2291

Table 1 *continued*

Table 1 (*continued*)

HJD	W_λ	σ
-2,450,000		
(d)	(mÅ)	(mÅ)
6248.8123	41.3750	1.2410
6254.8795	41.8054	1.2401
6260.7808	45.2798	1.2328
6289.7971	42.6745	1.2383
6361.6472	42.3128	1.2391
6401.5905	42.9964	1.2376
6417.5924	39.5673	1.2449
6607.8431	37.8184	1.2485
6612.8653	45.5610	1.2322
6656.7032	47.6766	1.2278
6659.7093	45.8957	1.2315
6664.6745	49.2717	1.2244
6670.7826	48.1998	1.2267
6672.8378	50.6189	1.2216
7038.7462	27.4097	1.2705
6677.7595	43.8922	1.2357
6687.7085	45.7443	1.2318
6690.6917	44.6191	1.2342
6697.7271	45.8772	1.2316
6698.7748	46.1766	1.2309
6710.6697	44.4810	1.2345
6712.6945	47.4635	1.2282
6718.7120	47.7831	1.2275
6725.5713	49.0575	1.2249
6729.5623	44.4447	1.2346
6732.6062	44.0142	1.2355
6739.5490	44.0139	1.2355
6746.5203	42.7372	1.2382
6750.5418	45.3872	1.2326
6754.5540	44.7233	1.2340
6765.5903	44.2191	1.2351
6766.5463	44.7315	1.2340
6767.5116	44.4612	1.2345
6774.5470	40.5219	1.2428
6775.4705	42.4427	1.2388
6777.5390	43.6835	1.2362
6781.4742	40.9965	1.2418
6786.5036	43.9414	1.2356
6787.5061	42.9262	1.2378

Table 1 *continued*

Table 1 (*continued*)

HJD	W_λ	σ
-2,450,000		
(d)	(mÅ)	(mÅ)
6791.5527	48.3870	1.2263
6795.5095	47.9230	1.2272
6800.4644	44.7013	1.2340
6801.5000	44.1911	1.2351
6802.5067	45.2528	1.2329
6803.5294	48.5563	1.2259
6806.5318	44.8490	1.2337
6807.6147	45.1985	1.2330
6809.4604	48.2952	1.2265
6810.4839	48.4599	1.2261
6811.4890	50.8294	1.2211
6818.5059	48.9579	1.2251
6819.5294	52.8926	1.2168
6823.5395	48.1640	1.2267
6824.5183	50.8258	1.2211
6825.5069	49.0499	1.2249
6829.4942	52.4642	1.2177
6832.5015	52.2552	1.2181
6833.5015	51.0414	1.2207
6835.5347	51.0836	1.2206
6836.4977	51.9177	1.2188
6837.4984	49.9543	1.2230
6838.5142	51.2240	1.2203
6839.5007	50.5233	1.2218
6840.4992	50.1879	1.2225
6845.4618	53.6993	1.2151
6847.4567	54.8509	1.2126
6850.5099	54.4124	1.2136
6855.4628	57.0751	1.2079
6856.4542	59.2667	1.2033
6857.4572	62.5979	1.1963
6858.4560	64.9401	1.1914
6859.4699	67.0792	1.1869
6863.4696	85.0692	1.1489
6864.4670	93.0745	1.1320
6866.5170	105.4488	1.1060
6867.4637	118.6766	1.0781
6870.4592	133.8580	1.0461
6871.4663	137.0995	1.0392

Table 1 *continued*

Table 1 (*continued*)

HJD	W_λ	σ
-2,450,000		
(d)	(mÅ)	(mÅ)
6872.4634	150.3551	1.0113
6873.4627	148.4821	1.0152
6874.4542	155.9589	0.9995
6876.4581	151.2320	1.0094
6878.4816	155.9124	0.9996
6879.4665	163.0676	0.9845
6880.4665	166.2434	0.9778
6881.4646	162.9879	0.9846
6882.4610	163.5481	0.9835
6883.4684	163.5807	0.9834
6885.4659	156.7293	0.9978
6886.4726	155.3184	1.0008
6887.4599	148.2345	1.0157
6941.9068	83.2774	1.1527
6942.9073	78.9372	1.1619
6943.9038	79.2119	1.1613
6950.8754	65.4337	1.1903
6951.8733	61.1214	1.1994
6952.8645	57.7236	1.2066
6953.8796	56.6173	1.2089
6954.8312	55.2559	1.2118
6955.8613	54.3239	1.2137
6956.8738	51.8092	1.2190
6957.8902	49.4740	1.2240
6958.8639	47.6115	1.2279
6959.8471	47.2173	1.2287
6961.8481	47.7860	1.2275
6964.8650	46.2104	1.2309
6965.8623	43.0701	1.2375
6968.8670	42.6636	1.2383
6969.8629	46.9872	1.2292
6972.8807	44.0054	1.2355
6974.8472	39.0575	1.2459
6977.8456	42.3540	1.2390
6979.8393	40.8341	1.2422
6980.8055	44.9754	1.2335
6982.8125	40.4891	1.2429
6984.8198	37.2191	1.2498
6985.8277	39.8160	1.2443

Table 1 *continued*

Table 1 (*continued*)

HJD	W_λ	σ
-2,450,000		
(d)	(mÅ)	(mÅ)
6986.8716	36.3258	1.2517
6988.7943	35.3878	1.2537
6990.7638	36.4655	1.2514
6992.7814	38.7161	1.2467
6994.8169	37.5105	1.2492
6996.8516	35.9668	1.2525
6998.8053	37.3780	1.2495
7000.8371	39.6315	1.2447
7007.8533	36.3848	1.2516
7008.7387	33.2607	1.2582
7009.7487	36.4337	1.2515
7012.8169	32.8265	1.2591
7013.8113	30.2994	1.2644
7014.7384	28.1325	1.2690
7015.7661	29.0392	1.2671
7016.7963	33.6223	1.2574
7018.7787	30.2510	1.2645
7021.8358	28.3041	1.2686
7022.7519	28.4105	1.2684
7025.8280	26.3324	1.2728
7026.7004	26.4958	1.2724
7030.6911	29.6624	1.2657
7032.8183	27.5399	1.2702
7035.7243	27.2459	1.2708
7037.8164	27.6261	1.2700
7038.8521	29.9518	1.2651
7039.8336	26.5309	1.2723
7040.7121	26.6035	1.2722
7043.8463	27.2521	1.2708
7046.6847	28.0830	1.2691
7047.6855	27.1237	1.2711
7048.8103	25.4844	1.2746
7050.7318	23.4698	1.2788
7051.8465	25.7026	1.2741
7059.7902	20.4370	1.2852
7060.6626	26.0203	1.2734
7061.8510	24.8567	1.2759
7062.6967	22.0224	1.2819
7063.7354	21.3341	1.2833

Table 1 *continued*

Table 1 (*continued*)

HJD	W_λ	σ
-2,450,000		
(d)	(mÅ)	(mÅ)
7064.7755	22.7382	1.2803
7068.7710	23.0571	1.2797
7070.6468	21.0678	1.2839
7074.8003	19.7124	1.2867
7075.6999	17.5518	1.2913
7078.8993	17.4877	1.2914
7083.6618	18.0506	1.2902
7088.6417	13.9511	1.2989
7091.5928	18.4445	1.2894
7092.7233	12.8638	1.3012
7093.7108	13.2399	1.3004
7095.8005	14.4630	1.2978
7097.6962	11.1866	1.3047
7104.5614	13.8121	1.2992
7115.7489	15.5300	1.2955
7118.5573	15.6659	1.2953
7120.5391	15.9264	1.2947
7124.4992	11.0033	1.3051
7125.5235	13.5067	1.2998
7127.6192	16.6063	1.2933
7130.5443	13.2235	1.3004
7132.5158	15.0305	1.2966
7134.6264	14.2428	1.2983

Table 2. + 87 km s⁻¹Measurements

HJD	W_λ	σ
-2,450,000		
(d)	(mÅ)	(mÅ)
5989.6915	6.9575	0.5690
5993.7546	6.4877	0.4666
6001.7288	7.0189	0.6171
6013.6892	6.7837	0.7300
6221.8876	5.6955	0.7066
6236.8436	6.1888	0.7984
6238.8674	5.4392	1.0361

Table 2 *continued*

Table 2 (*continued*)

HJD	W_λ	σ
-2,450,000		
(d)	(mÅ)	(mÅ)
6248.8123	5.6955	0.5610
6254.8795	6.2337	0.6488
6260.7808	5.5529	0.6005
6289.7971	6.2622	0.5882
6361.6472	6.8988	0.5884
6401.5905	6.8054	0.7523
6417.5924	7.6743	0.5769
6607.8431	6.4830	0.9925
6612.8653	7.0374	0.9321
6656.7032	6.1734	0.4011
6659.7093	6.5938	0.6570
6664.6745	7.5062	0.5782
6670.7826	6.2313	0.8487
6672.8378	6.1406	0.7884
7038.7462	8.8609	0.4875
6677.7595	5.5892	0.6148
6687.7085	5.3510	0.8682
6690.6917	6.9078	0.5528
6697.7271	7.8226	0.6497
6698.7748	6.5161	0.5798
6710.6697	5.6846	0.7924
6712.6945	6.5423	0.7655
6718.7120	7.1689	0.7073
6725.5713	5.9835	0.5270
6729.5623	7.7273	0.4005
6732.6062	6.9829	0.5528
6739.5490	7.1471	0.4769
6746.5203	7.0010	0.5962
6750.5418	7.6828	0.7995
6754.5540	6.2975	0.6330
6765.5903	7.2603	0.5293
6766.5463	7.4462	0.5885
6767.5116	6.5413	0.5541
6774.5470	6.1398	0.5976
6775.4705	6.0161	0.3171
6777.5390	6.1015	0.3593
6781.4742	6.5604	0.5276
6786.5036	6.0340	0.4806
6787.5061	6.0957	0.5503

Table 2 *continued*

Table 2 (*continued*)

HJD	W_λ	σ
-2,450,000		
(d)	(mÅ)	(mÅ)
6791.5527	6.0166	0.6992
6795.5095	7.2116	0.7634
6800.4644	7.1856	0.6102
6801.5000	5.8983	0.4060
6802.5067	4.9370	0.5346
6803.5294	6.3181	0.4875
6806.5318	3.6377	1.1296
6807.6147	4.3881	0.8387
6809.4604	5.4800	0.4523
6810.4839	6.5743	0.6446
6811.4890	5.4027	0.3113
6818.5059	5.9112	0.7276
6819.5294	6.4559	0.7309
6823.5395	5.9154	0.6874
6824.5183	7.5002	0.4767
6825.5069	5.7093	0.4808
6829.4942	4.9555	0.7242
6832.5015	5.5865	0.6765
6833.5015	5.4094	0.5411
6835.5347	5.4131	0.7196
6836.4977	6.0169	0.4646
6837.4984	5.8978	0.2831
6838.5142	5.1887	0.4357
6839.5007	5.1460	0.4750
6840.4992	5.0470	0.6156
6845.4618	5.2723	0.5693
6847.4567	6.2708	0.5228
6850.5099	5.0739	0.5690
6855.4628	3.2880	0.8426
6856.4542	5.3101	0.5070
6857.4572	5.4737	0.6054
6858.4560	5.6069	0.5388
6859.4699	5.2633	0.6833
6863.4696	6.1416	0.5253
6864.4670	4.3139	0.4121
6866.5170	2.9306	1.0689
6867.4637	5.1125	0.6642
6870.4592	3.9702	0.7236
6871.4663	3.4837	0.7023

Table 2 *continued*

Table 2 (*continued*)

HJD	W_λ	σ
-2,450,000		
(d)	(mÅ)	(mÅ)
6872.4634	4.8141	0.5248
6873.4627	4.5870	0.5503
6874.4542	6.1275	0.5268
6876.4581	5.5267	1.2326
6878.4816	7.1632	0.5748
6879.4665	5.3268	0.4990
6880.4665	5.7424	0.4804
6881.4646	5.5631	0.6196
6882.4610	6.3667	0.4998
6883.4684	5.2834	0.5567
6885.4659	3.5044	0.8973
6886.4726	3.7979	0.7180
6887.4599	5.4324	0.5923
6941.9068	5.5135	0.6352
6942.9073	6.0722	0.6552
6943.9038	7.4447	0.5162
6950.8754	7.1946	0.4945
6951.8733	8.1639	0.5595
6952.8645	8.1985	0.5905
6953.8796	8.2420	0.6296
6954.8312	9.3900	0.8081
6955.8613	8.3603	0.5537
6956.8738	9.1790	0.5338
6957.8902	8.5548	0.3678
6958.8639	7.9437	0.5608
6959.8471	8.5141	0.5679
6961.8481	9.3317	0.5193
6964.8650	8.7717	0.5678
6965.8623	8.9091	0.4967
6968.8670	9.1311	0.5058
6969.8629	8.4862	0.5019
6972.8807	9.0138	0.5930
6974.8472	9.0937	0.5025
6977.8456	8.9742	0.5387
6979.8393	7.3828	0.4877
6980.8055	8.8080	0.6131
6982.8125	9.3305	0.3660
6984.8198	9.3482	0.5050
6985.8277	9.0623	0.5774

Table 2 *continued*

Table 2 (*continued*)

HJD	W_λ	σ
-2,450,000		
(d)	(mÅ)	(mÅ)
6986.8716	9.2466	0.5336
6988.7943	8.7045	0.6594
6990.7638	8.9411	0.6907
6992.7814	9.3522	0.5176
6994.8169	8.3602	0.4506
6996.8516	7.8459	0.5787
6998.8053	9.0233	0.5028
7000.8371	9.0422	0.3881
7007.8533	8.0849	0.5467
7008.7387	9.1964	0.5310
7009.7487	9.7889	0.4396
7012.8169	8.1188	0.3972
7013.8113	9.5207	0.4539
7014.7384	9.6725	0.4726
7015.7661	11.3078	0.5339
7016.7963	10.3123	0.5559
7018.7787	9.5129	0.4672
7021.8358	9.3003	0.6022
7022.7519	9.6649	0.7746
7025.8280	9.2541	0.4911
7026.7004	9.5918	0.4978
7030.6911	10.5962	0.7018
7032.8183	9.7752	0.4993
7035.7243	9.6177	0.3830
7037.8164	9.6682	0.6541
7038.8521	9.6077	0.6162
7039.8336	8.6459	0.4043
7040.7121	9.6737	0.4904
7043.8463	10.5003	0.5425
7046.6847	9.5991	0.6591
7047.6855	9.0888	0.7053
7048.8103	9.1553	0.7067
7050.7318	9.3499	0.7276
7051.8465	9.5500	0.6863
7059.7902	10.4699	0.4528
7060.6626	10.3002	0.5673
7061.8510	10.8566	0.6771
7062.6967	9.5440	0.4022
7063.7354	9.0539	0.5210

Table 2 *continued*

Table 2 (*continued*)

HJD	W_λ	σ
-2,450,000		
(d)	(mÅ)	(mÅ)
7064.7755	10.3209	0.6899
7068.7710	8.5098	0.4984
7070.6468	11.1138	0.4044
7074.8003	9.9561	0.5636
7075.6999	10.5591	0.6446
7078.8993	10.1916	0.4279
7083.6618	11.6915	0.3053
7088.6417	9.5766	0.5989
7091.5928	11.7059	0.6554
7092.7233	10.3560	0.4098
7093.7108	10.5341	0.4324
7095.8005	11.3241	0.6450
7097.6962	9.0192	0.5465
7104.5614	11.1620	0.4707
7115.7489	11.3934	0.5647
7118.5573	11.2683	0.4354
7120.5391	10.2184	0.5184
7124.4992	12.2814	0.5199
7125.5235	9.8804	0.3943
7127.6192	10.3576	0.3959
7130.5443	10.3833	0.4921
7132.5158	9.5261	0.6126
7134.6264	10.3966	0.3892
8116.8606	5.2999	0.4137
8118.8165	5.4894	0.4418
8121.8505	4.9621	0.4014
8130.7972	5.2279	0.5254
8132.7853	4.2357	0.5714
8133.8294	4.8694	0.4552
8135.7970	5.0718	0.4733
8145.8177	5.7343	0.4658
8146.8286	5.2924	0.4023
8147.8066	5.9192	0.4301
8148.7815	5.9017	0.4739
8150.7582	5.3690	0.4648
8158.6342	5.7879	0.4606
8160.7501	5.8058	0.4439
8162.7974	6.0305	0.4349
8164.7352	5.5477	0.3781

Table 2 *continued*

Table 2 (*continued*)

HJD	W_λ	σ
-2,450,000		
(d)	(mÅ)	(mÅ)
8172.7982	6.0642	0.4702
8174.6811	5.8303	0.4847
8176.6893	6.1190	0.4063
8178.6189	6.1358	0.4895
8186.7597	5.9310	0.4177
8188.6939	5.6569	0.4698
8190.6400	5.7723	0.4124
8192.7439	5.8068	0.4421
8200.6405	5.7340	0.4374
8202.5807	5.7793	0.4124
8204.6013	4.9772	0.4790
8206.6028	4.9764	0.4171
8214.5330	5.6293	0.5741
8216.5715	5.2566	0.4795
8218.5708	4.5351	0.5933
8220.5664	5.1248	0.4728
8228.6131	4.9383	0.6416
8230.5611	4.8883	0.4610
8232.5621	4.9927	0.4078
8242.5156	4.8756	0.5288
8244.5167	4.7232	0.6114
8246.5215	4.1816	0.5869
8248.6102	4.1594	0.6660
8258.5731	4.6028	0.4507
8260.4913	4.1079	0.6641
8262.4987	4.7661	0.4661
8270.5720	3.1171	1.0923
8272.4622	4.4305	0.4789
8274.5431	4.2690	0.6600
8276.5334	3.7131	0.5313
8284.5375	4.2254	0.6119
8287.4957	4.8761	0.4310
8289.5123	4.1456	0.6214
8290.5663	4.9216	0.4633
8298.5078	4.0474	0.5453
8301.5267	4.8849	0.6908
8303.4741	4.4906	0.5030
8316.4768	4.4153	0.7053
8329.4678	4.8609	0.6449

Table 2 *continued*

Table 2 (*continued*)

HJD	W_λ	σ
-2,450,000		
(d)	(mÅ)	(mÅ)
8330.4688	4.7149	0.6765
8452.8630	4.5234	0.4178
8466.8571	4.4358	0.4701
8480.8632	4.7315	0.5157
8495.7624	3.6414	0.4933
8513.6726	3.5280	0.5242
8777.8660	5.3919	0.9074
8782.8819	5.8229	0.6407
8785.8744	4.7468	0.8103
8800.8592	6.3867	0.4662
8803.8497	6.1182	0.6688
8805.8312	6.8611	0.6851
8809.8619	6.5885	0.8066
8812.8630	6.1588	0.5554
8814.8574	6.4803	0.6234
8817.8610	5.7883	0.5637
8820.8104	6.1536	0.4876
8822.8133	6.0344	0.5743
8824.7950	6.0404	0.6142
8826.8360	5.7774	0.5780
8827.8608	6.2554	0.4869
8830.8214	6.2087	0.8675
8832.8593	6.9087	0.6375
8834.8460	6.7220	0.6081
8836.8174	5.8818	0.6183
8852.8207	5.7680	0.7024
8853.8375	6.5221	0.9110
8854.8133	5.1232	0.9352
8855.8436	5.9815	0.7943
8856.8048	5.7298	0.6826
8857.8663	5.2833	0.6781
8860.8514	5.1155	0.5466
8861.8533	6.2699	0.4861
8862.8308	5.6169	0.5726
8863.8699	5.6570	0.5895
8864.8254	6.8291	0.6214
8866.8648	5.3074	0.9421
8867.8760	5.1028	1.2621
8868.8816	5.4226	0.8160

Table 2 *continued*

Table 2 (*continued*)

HJD	W_λ	σ
-2,450,000		
(d)	(mÅ)	(mÅ)
8871.8362	5.1718	0.7734
8872.8191	5.1878	1.0159
8875.8653	5.3220	0.6858
8879.8167	5.3580	0.6493
8880.8738	5.9770	0.7499
8881.8639	5.4094	0.6616
8882.8219	5.4810	0.6340
8883.8449	5.9745	0.7162
8884.7985	6.0315	0.6037
8886.8221	5.4267	0.5306
8887.8172	5.9484	0.4732
8888.8627	5.9402	0.5647
8889.8636	5.9201	0.5624
8890.8608	5.2729	0.5544
8891.8962	5.4412	0.5985
8892.8507	4.8640	0.7056
8893.8244	5.5802	0.5533
8894.8883	5.0969	0.6055
8895.7919	6.8546	0.7473
8896.8512	5.1043	0.7421
8897.7793	4.7744	0.5408
8898.7409	4.9412	0.5014
8899.7816	5.3626	0.5083
8900.7151	5.4527	0.5108
8901.7245	5.1093	0.5539
8902.7389	5.4294	0.6548
8903.7444	4.8602	0.5707
8904.7448	5.0492	0.5340
8905.7200	4.6773	0.5662
8906.7154	5.2632	0.5417
8907.7330	5.0922	0.5449
8908.7334	5.0118	0.4672
8909.7035	4.7002	0.5172
8910.7072	6.0793	0.5556
8911.6643	4.9627	0.5609
8912.6790	4.9955	0.5705
8914.7153	4.5219	0.6795
8915.7889	5.7322	0.6033
8916.7380	4.9506	0.6643

Table 2 *continued*

Table 2 (*continued*)

HJD	W_λ	σ
-2,450,000		
(d)	(mÅ)	(mÅ)
8917.7593	6.3266	0.5666
8918.6995	5.4386	0.5988
8919.6849	5.6215	0.6395
8920.7120	5.3495	0.5328
8921.7181	5.4387	0.5980
8922.6421	4.2238	0.8165
8923.6323	5.0022	0.6467
8924.6323	4.7297	0.5665
8925.6034	5.2500	0.4730

Table 3. — 168 km s⁻¹ Measurements

HJD	W_λ	σ
-2,450,000		
(d)	(mÅ)	(mÅ)
8116.8606	1.9270	2.0744
8118.8165	2.7298	2.2157
8121.8505	2.8522	2.0058
8130.7972	3.1699	2.6286
8132.7853	5.9941	2.8296
8133.8294	3.0175	2.2726
8135.7970	4.1528	2.3626
8145.8177	2.9724	2.3386
8146.8286	3.7882	2.0119
8147.8066	3.0426	2.1619
8148.7815	3.7487	2.3795
8150.7582	5.8807	2.3191
8158.6342	4.8814	2.3076
8160.7501	4.5840	2.2253
8162.7974	6.5519	2.1777
8164.7352	6.0477	1.8886
8172.7982	4.8312	2.3603
8174.6811	4.9278	2.4292
8176.6893	4.6321	2.0407
8178.6189	6.9212	2.4517
8186.7597	6.5458	2.0901

Table 3 *continued*

Table 3 (*continued*)

HJD	W_λ	σ
-2,450,000		
(d)	(mÅ)	(mÅ)
8188.6939	5.0281	2.3515
8190.6400	4.6226	2.0666
8192.7439	6.2721	2.2111
8200.6405	5.5918	2.1889
8202.5807	5.0442	2.0657
8204.6013	3.7935	2.3908
8206.6028	4.1444	2.0806
8214.5330	4.9041	2.8736
8216.5715	4.5730	2.3948
8218.5708	1.7513	2.9603
8220.5664	3.9028	2.3617
8228.6131	1.8869	3.2091
8230.5611	1.9861	2.3046
8232.5621	1.5371	2.0417
8242.5156	3.1707	2.6394
8244.5167	1.8863	3.0541
8246.5215	1.5284	2.9227
8248.6102	4.5160	3.3030
8258.5731	3.2661	2.2456
8260.4913	1.5134	3.3055
8262.4987	5.1208	2.3189
8270.5720	2.3722	5.3956
8272.4622	4.1881	2.3804
8274.5431	6.3511	3.2676
8276.5334	2.2828	2.6348
8284.5375	3.0182	3.0421
8287.4957	3.3950	2.1505
8289.5123	3.1830	3.0871
8290.5663	3.3647	2.3125
8298.5078	1.8562	2.7121
8301.5267	1.5341	3.4561
8303.4741	1.9703	2.5084
8316.4768	0.6062	3.5221
8329.4678	1.2385	3.2268
8330.4688	1.4468	3.3811
8452.8630	0.6586	2.0873
8466.8571	0.8109	2.3471
8480.8632	4.0911	2.5686
8495.7624	3.6353	2.4410

Table 3 *continued*

Table 3 (*continued*)

HJD	W_λ	σ
-2,450,000		
(d)	(mÅ)	(mÅ)
8513.6726	-2.7691	2.6141
8777.8660	-5.9810	4.0175
8782.8819	-3.0090	2.8326
8785.8744	-2.9033	3.5581
8800.8592	-1.7399	2.0647
8803.8497	-1.1761	2.9545
8805.8312	0.6667	3.0328
8809.8619	-0.0915	3.5684
8812.8630	0.1391	2.4498
8814.8574	-2.3675	2.7647
8817.8610	0.8139	2.4784
8820.8104	-1.0610	2.1543
8822.8133	-2.1444	2.5394
8824.7950	-1.8230	2.7145
8826.8360	-2.8950	2.5544
8827.8608	-3.0781	2.1587
8830.8214	-2.6295	3.8425
8832.8593	-4.6527	2.8437
8834.8460	-2.8550	2.7029
8836.8174	-2.4430	2.7322
8852.8207	-4.9671	3.1129
8853.8375	-6.8060	4.0663
8854.8133	-4.2678	4.1242
8855.8436	-4.4630	3.5223
8856.8048	-3.0746	3.0165
8857.8663	-5.2199	2.9973
8860.8514	-6.9145	2.4193
8861.8533	-5.2517	2.1616
8862.8308	-4.4471	2.5336
8863.8699	-4.7974	2.6102
8864.8254	-8.5891	2.7861
8866.8648	-3.8925	4.1570
8867.8760	-0.3216	5.5342
8868.8816	-3.8268	3.6030
8871.8362	-2.9384	3.4052
8872.8191	-0.2323	4.4564
8875.8653	-4.8696	3.0303
8879.8167	-2.7358	2.8614
8880.8738	-5.1024	3.3282

Table 3 *continued*

Table 3 (*continued*)

HJD	W_λ	σ
-2,450,000		
(d)	(mÅ)	(mÅ)
8881.8639	-5.5478	2.9277
8882.8219	-5.6743	2.8073
8883.8449	-0.6598	3.1591
8884.7985	-0.0741	2.6614
8886.8221	3.9531	2.3174
8887.8172	5.0786	2.0700
8888.8627	6.3572	2.4656
8889.8636	9.5681	2.4444
8890.8608	10.0664	2.3980
8891.8962	13.8973	2.5777
8892.8507	13.7307	3.0286
8893.8244	14.5997	2.3825
8894.8883	18.3980	2.5852
8895.7919	18.3334	3.2259
8896.8512	17.4236	3.1734
8897.7793	19.9830	2.2992
8898.7409	21.6081	2.1290
8899.7816	21.2090	2.1652
8900.7151	20.9040	2.1779
8901.7245	23.4560	2.3480
8902.7389	21.8435	2.7880
8903.7444	24.7157	2.4112
8904.7448	21.7421	2.2686
8905.7200	21.6379	2.4001
8906.7154	23.8953	2.2970
8907.7330	23.4400	2.3098
8908.7334	21.2560	1.9855
8909.7035	24.2127	2.1845
8910.7072	22.5546	2.3726
8911.6643	21.9787	2.3805
8912.6790	21.3513	2.4242
8914.7153	20.7693	2.8814
8915.7889	22.1137	2.5725
8916.7380	23.4706	2.8134
8917.7593	22.4455	2.4234
8918.6995	18.3622	2.5623
8919.6849	19.5739	2.7347
8920.7120	20.1201	2.2729
8921.7181	18.0060	2.5603

Table 3 *continued*

Table 3 (*continued*)

HJD	W_λ	σ
-2,450,000		
(d)	(mÅ)	(mÅ)
8922.6421	18.7528	3.4659
8923.6323	18.1697	2.7605
8924.6323	19.4647	2.4099
8925.6034	17.4798	2.0244